Localized Delivery of Theranostic Nanoparticles and High-Energy Photons using Microneedles-on-Bioelectronics

Youngsik Lee, Taegyu Kang, Hye Rim Cho, Gil Ju Lee, Ok Kyu Park, Sangyeon Kim, Bowon Lee, Hyun Myung Kim, Gi Doo Cha, Yoonsoo Shin, Wanghee Lee, Minjeong Kim, Hyunjoong Kim, Young Min Song,* Seung Hong Choi,* Taeghwan Hyeon,* and Dae-Hyeong Kim*

The low delivery efficiency of light-responsive theranostic nanoparticles (NPs) to target tumor sites, particularly to brain tumors due to the blood–brain barrier, has been a critical issue in NP-based cancer treatments. Furthermore, high-energy photons that can effectively activate theranostic NPs are hardly delivered to the target region due to the strong scattering of such photons while penetrating surrounding tissues. Here, a localized delivery method of theranostic NPs and high-energy photons to the target tumor using microneedles-on-bioelectronics is presented. Two types of microneedles and flexible bioelectronics are integrated and mounted on the edge of surgical forceps. Bioresorbable microneedles containing theranostic NPs deliver the NPs into target tumors (e.g., glioblastoma, pituitary adenoma). Magnetic resonance imaging can locate the NPs. Then, light-guiding/spreading microneedles deliver high-energy photons from bioelectronics to the NPs. The high-energy photons activate the NPs to treat tumor tissues by photodynamic therapy and chemotherapy. The controlled thermal actuation by the bioelectronics accelerates the diffusion of chemo-drugs. The proposed method is demonstrated with mouse tumor models in vivo.

1. Introduction

Stimuli-responsive theranostic nanoparticles (NPs) have a potential for the local treatment of cancers while minimizing unwanted side effects of damaging other normal tissues.[1] The interplay between theranostic NPs and external stimuli results in physicochemical changes of the NPs, which induces release and/or activation of theranostic agents. Among various types, light-responsive theranostic NPs have been widely studied. The facile spatiotemporal control over the activation of the NPs and the release of therapeutic payloads by the light have been reported,[2] while vicinal side effects, such as unintended thermal, chemical, or electrical damages, have been avoided.

However, these theranostic NPs, typically injected via intravenous routes, have suffered from their low efficiency of reaching target tumor sites. It is particularly a critical issue for the NPs targeting brain tumors due to the blood–brain barrier (BBB).[3] The BBB is an essential protective barrier that protects the central nervous system from external pathogens and also blocks the delivery of theranostic NPs into the brain. Therefore, a novel method for the localized delivery of theranostic NPs by detouring the BBB is needed to treat the brain tumor effectively.[4]

To activate the theranostic NPs, long-wavelength lights such as red light and/or near-infrared (NIR) light have been used owing to their deep penetration depth in biological tissues.[5] However, the low energy photons are often not enough

Dr. Y. Lee, Dr. T. Kang, Dr. H. R. Cho, Dr. O. K. Park, S. Kim, B. Lee,
G. D. Cha, Y. Shin, W. Lee, M. Kim, H. Kim, Prof. S. H. Choi,
Prof. T. Hyeon, Prof. D.-H. Kim
Center for Nanoparticle Research
Institute for Basic Science (IBS)
Seoul 08826, Republic of Korea
E-mail: verocay1@snu.ac.kr; thyeon@snu.ac.kr; dkim98@snu.ac.kr
Dr. Y. Lee, Dr. T. Kang, S. Kim, B. Lee, G. D. Cha, Y. Shin, W. Lee, M. Kim,
H. Kim, Prof. T. Hyeon, Prof. D.-H. Kim
School of Chemical and Biological Engineering
Institute of Chemical Processes
Seoul National University
Seoul 08826, Republic of Korea

The ORCID identification number(s) for the author(s) of this article can be found under https://doi.org/10.1002/adma.202100425.

Dr. H. R. Cho, Dr. O. K. Park, Prof. S. H. Choi
Department of Radiology
Seoul National University College of Medicine
Seoul 03080, Republic of Korea
Dr. G. J. Lee, H. M. Kim, Prof. Y. M. Song
School of Electrical Engineering and Computer Science (EECS)
Gwangju Institute of Science and Technology (GIST)
Gwangju 61005, Republic of Korea
E-mail: ymsong@gist.ac.kr

Prof. D.-H. Kim
Department of Materials Science and Engineering
Seoul National University
Seoul 08826, Republic of Korea

**ADVANCED
SCIENCE NEWS**

www.advancedsciencenews.com

**ADVANCED
MATERIALS**

www.advmat.de

to efficiently activate various theranostic functions of the NPs. Although there have been several approaches proposed to solve this insufficient energy issue, such as the upconversion or multiphoton-activation method,[6] the efficiency of such methods to boost the energy of the delivered light still needs further improvement. Therefore, the deficient light energy to activate theranostic NPs presents a challenging research topic.

On the contrary, short-wavelength light sources such as blue light and/or ultraviolet (UV) light exhibit high efficiency for the activation of the NPs due to their high energy.[7] Thus, their application can be a potential solution for the low energy issue of long-wavelength lights. Protoporphyrin and Ce6 dyes for the photodynamic therapy (PDT) absorb light energy far more efficiently when activated by UV light ($\approx$365 nm; 3.4 eV) than red light ($\approx$650 nm; 1.9 eV).[8] However, the delivery of such high-energy photons to theranostic NPs deep inside the target tumor is difficult due to the scattering and absorption of the high-energy photons by surrounding tissues and fluids.

2. Results and Discussion

We herein present a localized delivery method of theranostic NPs and high-energy photons using microneedles-on-bioelectronics. Besides transdermal delivery, microneedles have been widely studied for the delivery of therapeutic payload or diagnosis due to their effective penetration into the target site.[9] The high-energy photons are used to activate the theranostic NPs that are locally delivered to the target tumor (e.g., glioblastoma, pituitary adenoma). For the localized delivery of theranostic NPs and high-energy photons, two types of functionalized microneedles and the flexible bioelectronics are integrated and mounted on the minimally invasive surgical forceps. **Figure 1** describes the proposed method. The step-by-step procedures are depicted in Figure S1 (Supporting Information).

First, the hyaluronic-acid-based bioresorbable microneedles (BMNs) containing theranostic NPs are administered to the target tumor region (Figure 1a). After penetrating the tumor tissue, the BMNs are dissolved by biofluids, and the NPs are locally delivered into the tumor (Figure 1b). Whereas the BBB limits the intravenous delivery of the NPs to the brain, this
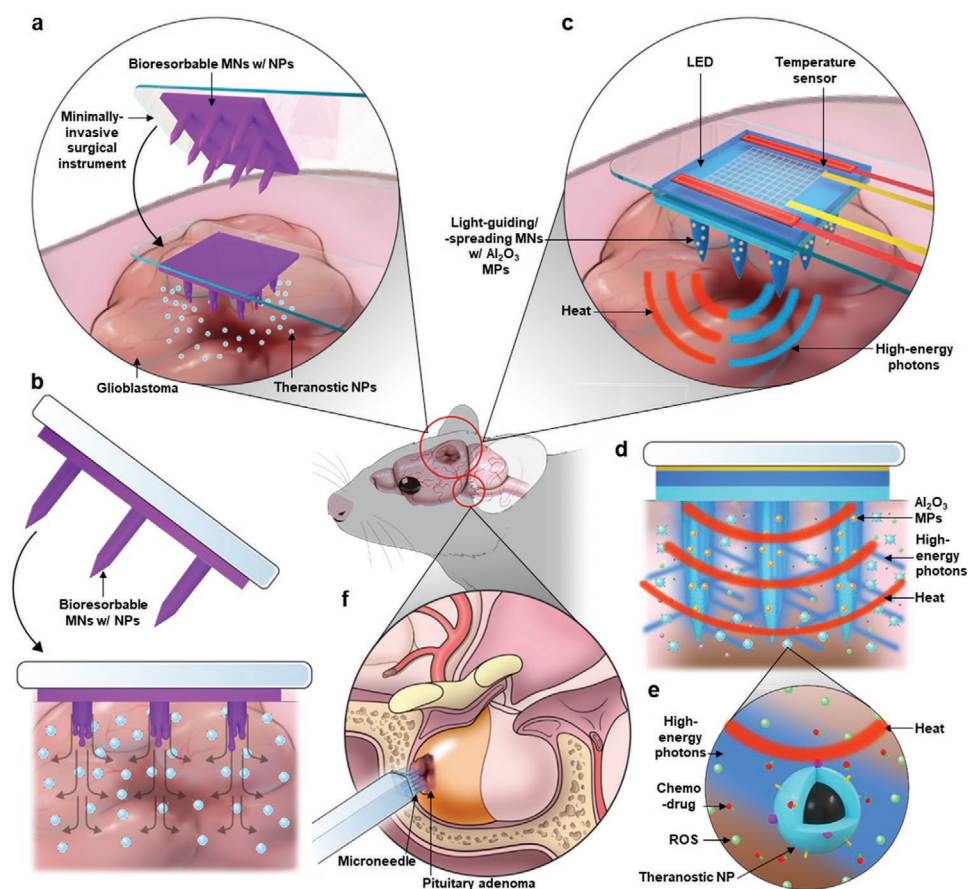

Figure 1. Localized delivery of theranostic NPs and their activation by high-energy photons. a) Localized delivery of theranostic NPs to glioblastoma bypassing the BBB by using BMNs. b) Biodegradation of the BMNs and release of the NPs inside the target tumor. c) Delivery of the high-energy photons via the LMNs with Al_2O_3 microparticles (MPs) and controlled application of the heat by the bioelectronics. d) Activation of the NPs by the high-energy photons and accelerated diffusion of the therapeutic agents by the controlled thermal actuation. e) Release of the ROS and Dox from the NPs by the irradiation of the high-energy photons. f) Application of the proposed method to the minimallyinvasive treatment of pituitary adenoma.

localized delivery method allows the NPs to bypass the BBB and be delivered to the target brain tumor (e.g., glioblastoma). The thin thickness of the forceps minimizes the size of the surgical incision, which reduces the associated pain and recovery time.

Second, the epoxy-based light-guiding/spreading microneedles (LMNs) integrated with the flexible bioelectronics are administered to the target brain region (Figure 1c). For the application of the LMNs, the delivered theranostic NPs can be located by imaging tools such as magnetic resonance (MR) imaging. The high-energy photons (3.4 eV) are generated by the light-emitting diode (LED) in the bioelectronics, and the LMNs guide the generated photons to the NPs inside the tumor. The alumina (Al_2O_3) microparticles embedded in the LMNs can scatter and diffuse the guided photons to nearby tumor tissues (Figure 1d). The LMNs with microparticles not only guide but also spread high-energy photons inside the tumor tissues. The delivered high-energy photons activate the theranostic NPs.

The multifunctional theranostic NP consists of an iron oxide core and a mesoporous silica shell doped with PDT dyes. On the surface of the shell, linkers are grafted to conjugate chemotherapy drugs (e.g., Doxorubicin (Dox)). The core is used for MR imaging. By the irradiation of high-energy photons, the PDT agents generate reactive oxygen species (ROS) on the NP surface, and the Dox are released from the NP surface by the photochemical cleavage of linkers (Figure 1e). Because of the short lifetime of ROS in biological systems, the locally generated ROS effectively treat target tumor but rarely induce damage to nearby normal tissues.[10] The heat generated from the LED, which is controlled by the temperature sensor in the bioelectronics, enhances the diffusion of therapeutic moieties inside tumor tissues by increasing the diffusivity as well as the cell membrane permeability (Figure 1d).[11]

Besides glioblastoma, the same method can also be applied to other types of brain tumors such as pituitary adenoma (Figure 1f). Pituitary adenoma is a tumor that occurs in the adenohypophysis of the pituitary gland. Under the oncogenesis of pituitary adenoma, an excessive amount of hormones is secreted, which induces various complications.[12] The minimally invasive resection surgery is generally employed for the removal of pituitary adenoma. In this procedure, a camera-equipped endoscope with thin surgical forceps is inserted to visualize and remove pituitary adenoma.[13] However, there is a potential risk in the conventional surgical approach because normal pituitary gland tissues near the adenoma might be damaged during the surgical resection procedure due to its small size.[13a] The microneedle-based treatment can avoid and/or minimize such a risk.

The detailed synthetic protocol of theranostic NPs is described in the Supporting Methods (Supporting Information). Cetyltrimethylammonium bromide is used for the transfer of as-synthesized hydrophobic iron oxide NPs from organic medium to aqueous phase and the formation of mesopores. After addition of tetraethyl orthosilicate, and protoporphyrin IX–(3-aminopropyl)triethoxysilane to form the silica shell, the shell surface is functionalized with amine-groups and thiol-groups. Amine-groups and thiol-groups are conjugated with photolabile linker and poly(ethylene glycol), respectively. After the reaction of amine-groups at the photolabile linker on silica shell with succinic anhydride to form carboxylic acid moiety, Dox is immobilized on theranostic NPs.

BMNs are fabricated by the two-step molding process (**Figure 2**a). A mixture of hyaluronic acid and theranostic NPs in deionized water (DI water) is poured into a prefabricated mold, and the trapped air in the mold is removed by applying a vacuum. After microneedle mold is filled with the solution without voids, DI water in the base solution is evaporated. Then, solidified microneedles in the mold are detached from the mold.

The BMN is designed to have a dimension of 0.25 mm × 2 mm (diameter × length; individual microneedle) and an interneedle space of 2 mm (Figure 2b). The fluorescence images of a microneedle containing the PDT dye (green) doped on the NPs and the Dox (red) loaded on the NPs (Figure 2c left and right, respectively) show the uniform distribution of the theranostic NPs inside the BMN. The images also confirm that the tip of the fabricated microneedle has a sharp edge for the facile penetration of the microneedles into the target tissue.

BMNs are mechanically sturdy enough to smoothly penetrate the target tumor tissue without mechanical damages to the BMNs during the insertion procedure. The mechanical strength of the BMNs is estimated by the compression test (Figure 2d). Metal weights are placed on the BMNs to apply the external force along the vertical direction. Maximum pressures that the sharp edge (i.e., 0–1.1 mm) and pillar (1.1–2 mm) of the BMNs can endure are 1.4 and 13.8 MPa, respectively, which are high enough to penetrate the soft brain tissue including the brain tumor tissue (e.g., Young's modulus of the brain and the brain tumor are 7.4 and 11.4 kPa[14]).

For further characterization, BMNs are applied to the artificial brain tissue that consists of 0.6% agar gel, fabricated by following the previously reported method.[15] BMNs smoothly penetrate the artificial brain tissue, which confirms the mechanical strength of the BMNs (Figure 2e). As BMNs are inserted into the artificial tissue, they are dissolved by biofluids within 1–2 min (Figure 2f). By applying high-energy photons (3.4 eV) to the delivered theranostic NPs by the dissolution of BMNs, the loaded Dox can be released from the NPs. Figure 2g shows the release and diffusion of the Dox to the nearby artificial tissue by the irradiation of the high-energy photons for 20 min at 37 °C. Drugs (Dox; red fluorescence) are confined in the NPs without the irradiation of photons (Figure 2g, left), whereas they are released by the irradiation (Figure 2g, right). More quantitative plots for analyzing the fluorescent signal intensity can be found in Figure S2b (Supporting Information).

The theranostic agents from the NPs can diffuse naturally due to the concentration gradient. Nevertheless, such mass transfer based on the natural diffusion is quite slow. Therefore, thermal actuation is utilized to accelerate the mass transfer. The measurement setup using the confocal microscope and its focusing position to observe the drug diffusion inside the artificial tissue is illustrated in Figure 2h (more details in Figure S3, Supporting Information). Figure 2i,j shows diffused drugs (Dox; red fluorescence) under 37 and 47 °C after 20 min near the edge of the BMNs. The diffusion of Dox is slow at 37 °C, and the interneedle space is partially filled with the diffused drug molecules (Figure 2i). However, the thermal actuation ($\Delta T = 10$ °C) can accelerate the drug diffusion so that the drugs can spread and fill the inter-needle space more rapidly (Figure 2j). More
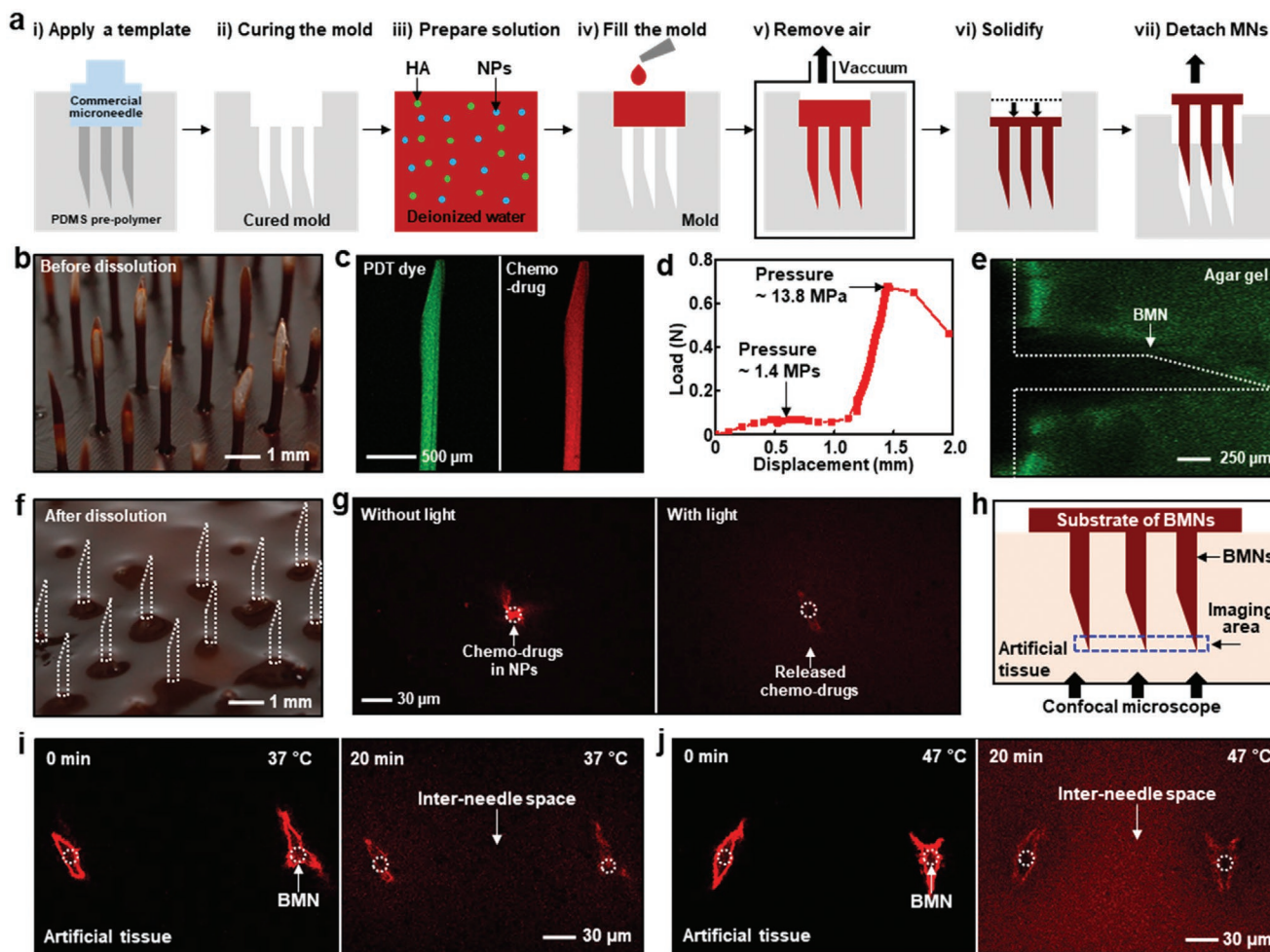
Figure 2. Fabrication, design, and characterization of BMNs. a) Schematic illustrations that show the fabrication process of BMNs using the cured mold. b) Optical camera image of BMNs. c) Fluorescence microscopy image of a BMN with the PDT dye (left) and that with the Dox (right). The PDT dye and Dox are doped or grafted on the theranostic NPs and then loaded inside the BMNs. d) Compression test (load–displacement curve) of the BMNs by applying the metal weights on the BMNs. e) Fluorescence microscopy image of a BMN that penetrates the artificial brain tissue. f) Optical camera image of the plate of the BMN after the dissolution of microneedles. The white dotted boxes show the location of BMNs before their dissolution. g) Release and diffusion of Dox from the theranostic NPs without (left) and with (right) the irradiation of high-energy photons from the bioelectronics. h) Measurement position of the fluorescence image to observe the diffusion of the Dox using confocal microscopy. i,j) Fluorescence microscopy images for observing the drug diffusion in the artificial tissue by the irradiation of high-energy photons for 20 min at 37 °C (i) and 47 °C (j).

quantitative plots for analyzing the fluorescent signal intensity can be found in Figure S2d, S2f (Supporting Information).

LMNs are made of a photocurable transparent polymer (epoxy; NOA63, Norland Products Inc., USA), and Al_2O_3 microparticles are embedded inside the LMNs (**Figure 3**a,b for the optical and scanning electron microscope (SEM) images, respectively). The fabrication method of LMNs is similar to that of BMNs (see the Supporting Methods, Supporting Information). The LMNs have a dimension of 0.3×3 mm (diameter × length; individual microneedle) and an interneedle space of 2 mm. The longer length of LMNs than that of BMNs is favorable for the delivery of photons to the diffused NP. The Al_2O_3 microparticle has a diameter of 1 µm and a refractive index of ≈1.8 at the operating wavelength.[16] The LMNs with Al_2O_3 microparticles guide and spread high-energy photons into the target tissue, and the high-energy photons activate the

theranostic NPs inside the tumor. The sharp needle-like shape of the microneedle is efficient at penetrating the cancer tissue.

In particular, the Al_2O_3 microparticles embedded in the LMNs play an essential role in the scattering and diffusion of the guided photons. According to the optical simulation, the microparticles induce the strong Mie scattering under the wavelength of 365 nm (Figure 3c).[17] The microparticle with optimum material properties (e.g., $n = 1.8$ and diameter = 1 µm) scatters the incident UV light strongly (Figure 3d). Detailed conditions and methods for the optical analysis, including the development of the optical simulation model, are described in Supporting Methods and Figure S4 (Supporting Information). The guided photons spread to nearby tissues due to the light scattering. The scattering enables the photons to overcome the total internal reflection at the interface between the microneedle and the tissue in the absence of microparticles (Figure 3e). In
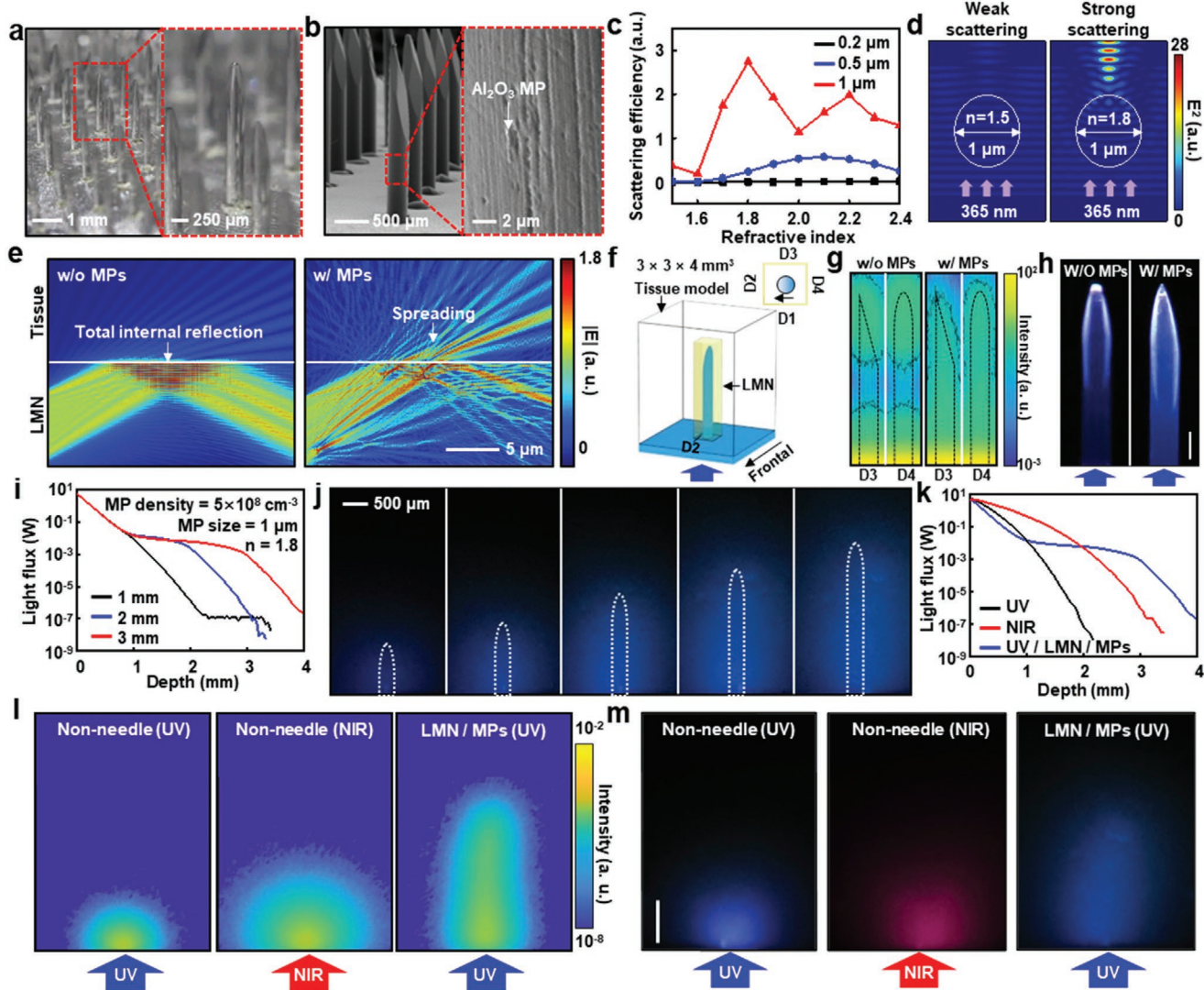
**ADVANCED
SCIENCE NEWS**

www.advancedsciencenews.com

**ADVANCED
MATERIALS**

www.advmat.de

Figure 3. Design and characterization of LMNs. a) Optical images of LMNs. b) SEM images of LMNs. c) Optical simulation of the scattering efficiency by the Al$_2$O$_3$ microparticles (MPs) with various refractive indices and diameters. d) Electric field distributions of the scattered light by the single microparticles with the refractive index of 1.5 (left) and 1.8 (right), respectively. e) Electric field simulation at the interface between the microneedle and the tissue for the LMN without (left) and with (right) the microparticles. The refractive index of tissue is set as 1.36. f) Schematic illustration of the model for the optical simulation to visualize the light-guiding and light-spreading by the LMN. g) Light distributions captured by two domains (i.e., D3 and D4): LMN without (left) and with (right) microparticles. The microparticle concentration is set as 5×10^8 cm^{-3}. h) Photographs of the LMN without (left) and with (right) the microparticles (scale bar = 0.3 mm). i) Simulated depth profile of the light flux in the brain tissue depending on the length of the LMN. j) Measurement of the light delivered into the optical phantom by the LMN with microparticles depending on the length of the LMN. k) Simulated depth profile of the light flux in the brain tissue. l) Optical simulation of the light penetration into the brain tissue for three cases: direct UV irradiation without LMNs (left; scale bar = 1 mm), direct NIR irradiation without LMNs (middle), and UV delivery through LMNs with microparticles (right). m) Optical camera images of the optical phantom for three cases: details are the same as those of Figure 3l.

addition, the parallel propagating light, which does not spread with the LMN only, can be effectively diffused by the LMN with the microparticles (Figure S5, Supporting Information).

To further investigate the light-spreading by the LMN with microparticles, another simulation model was set as shown in Figure 3f. Four simulation domains that surround the LMN with a distance of 150 μm capture the diffused light. According to the light distribution obtained in the parametric studies, the optimized concentration and size of the microparticles are 5×10^8 cm^{-3} and 1 μm, respectively (Figure S6, Supporting

Information). The simulation results exhibit that the LMN without microparticles concentrates the light at the tip, whereas the LMN with microparticles spreads the light throughout the microneedle (Figure 3g; and Figure S7a, Supporting Information). Optical camera images of the microneedle support the simulation results (Figure 3h). The guided light is focused at the edge of the LMN without microparticles, but the light spreads throughout the microneedle including the pillar of the LMN with microparticles. Figure 3i; and Figure S7b (Supporting Information) exhibit the calculated light flux delivered to the tissue

by the LMN depending on the length of the LMN (with 365 nm light). Because the total light flux and the light penetration depth increase as the length of the LMN becomes longer according to the simulation, the longest length of the LMN (3 mm long) was selected. Also, the experimental results using the custom-made optical phantom confirm that the longer LMN delivers the light deeper (Figure 3j). Details for the optical measurement and the fabrication of the optical phantom are described in Supporting Methods and Figure S8 (Supporting Information).

The calculated flux of the light delivered by the LMN with microparticles is much higher than control cases (i.e., UV or NIR delivery without LMNs), particularly at the deep tissue regions (Figure 3k). For example, Figure 3l compares the calculated light distributions of three cases: 1) UV delivery without the LMNs (control), 2) NIR delivery without the LMNs (control), and 3) UV delivery via the LMNs with microparticles. The UV photons cannot reach over ≈1 mm depth without LMNs due

to their scattering and absorption by the tissue. The NIR photons can penetrate ≈2 mm since the scattering and absorption of the NIR light are lower than those of the UV light. Despite the deeper penetration of NIR, its energy can still be insufficient to activate the theranostic NPs.[18] On the other hand, the LMNs with microparticles deliver the high-energy photons more deeply (≈3 mm), even more than the NIR case. The experimental results of three cases (Figure 3m) support the simulation results (Figure 3l). Therefore, the activation of theranostic NPs by UV photons at the deep tissue region can be achieved using the LMNs with Al_2O_3 microparticles.

The theranostic NP consists of two parts, the iron oxide NP core used for the MR imaging and the mesoporous silica shell on which the PDT dyes and Dox are loaded for photoactive treatments (**Figure 4**a). The uniform size of the core and the mesoporous structure of the shell are observed by the transmission electron microscopy (Figure S9a,b Supporting
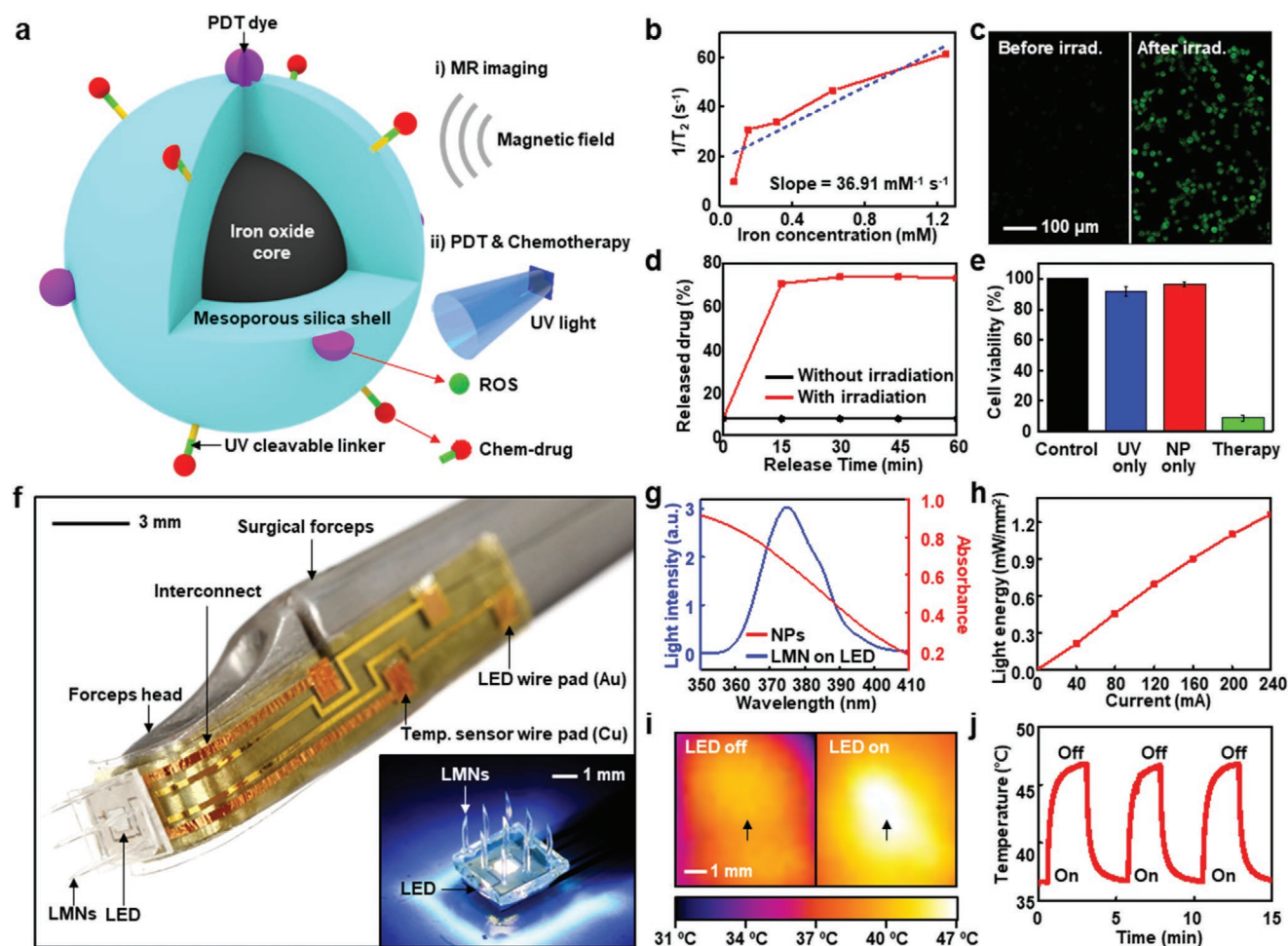

Figure 4. Design and characterization of theranostic NPs and microneedles-on-bioelectronics. a) Schematic illustration of the theranostic NP. b) R_2 relaxivity change of the theranostic NP at various iron concentrations, measured with a 3T MR scanner. c) Relative intracellular ROS generation by theranostic NPs measured from the fluorescence intensity change of DCFH-DA before (left) and after (right) the irradiation. d) Time-dependent drug release profile from the theranostic NPs without (control) and with (experiment) the irradiation of high-energy light (3.4 eV). e) Cell viability (U-87 MG cells) result of the control group, the "UV only" group, the "NPs only" group, and the therapy group. f) Photograph of the microneedles-on-bioelectronics attached on the tip of the surgical forceps. The inset shows the light emission from LMNs integrated on the LED. g) Wavelength-dependent intensity of the emitted light from LMNs integrated on the LED and the typical light absorbance by the theranostic NPs. h) The energy of the emitted light can be controlled by the applied current to the LED. i) Infrared camera images of the artificial tissue when the LED is turned on (right) and off (left). j) Cyclic temperature change profile.

**ADVANCED
SCIENCE NEWS**

www.advancedsciencenews.com

**ADVANCED
MATERIALS**

www.advmat.de

Information). The presence of iron ions at the core and silicon ions at the shell is analyzed with energy-dispersive X-ray spectroscopy (Figure S9c, Supporting Information). After dispersion in water, the hydrodynamic diameter of NPs, measured by the dynamic light scattering, is 115 nm (Figure S9d, Supporting Information). The transverse (r_2) relaxivity of theranostic NPs is measured using a 3 T preclinical MR scanner. The r_2 relaxivity of 36.9×10^{-3} M^{-1} s^{-1} is determined from the relaxation rate (R_2) variation of the theranostic NPs with various iron concentrations (Figure 4b). T_2-weighted MR images of the optical phantom that contains theranostic NPs with various concentrations show that the MR signal intensity attenuates as the concentration of the NPs increases (Figure S9e, Supporting Information).

Based on this NP platform, two kinds of photoactive therapeutic moieties, the PDT dye (e.g., protoporphyrin) and the Dox with the photoresponsive linker, are loaded on the NPs for the localized light-responsive cancer treatment. Details for the synthesis and characterization of NPs are described in Methods Section (Supporting Information). We characterized the therapeutic performance of the synthesized NPs in vitro as follows.

The intracellular generation of ROS by theranostic NPs under the absorption of delivered high-energy photons is observed in human primary glioblastoma cells (U-87 MG) using confocal microscopy. The ROS-sensitive probe (2′,7′-dichlorofluorescin diacetate; DCFH-DA) is employed to estimate the intracellular ROS generation from fluorescence intensity changes.

After the irradiation of high-energy photons, the strong fluorescence is observed, which indicates that the NPs effectively generate ROS in vitro (Figure 4c).

The Dox is covalently linked to the NP via a photoresponsive linker. The absorption of the high-energy photons causes the phototriggered cleavage of the linker to release loaded Dox from the NP. The in vitro drug release profiles from the theranostic NPs without or with the irradiation of high-energy photons are investigated by monitoring the chemo-drug concentration with UV–vis absorption spectroscopy (Figure 4d; and Methods Section, Supporting Information). The results showed that more than 60% of the chemo-drug is released with the light irradiation, while NPs without the light irradiation show negligible drug release. These indicate that the light-driven activation of the NPs enables the precisely controlled drug delivery while minimizing the leakage of loaded drugs in the absence of the light irradiation.

The treatment efficacy of the photo-triggered NPs against the glioblastoma cells was evaluated by using the live/dead cell viability assay in vitro. As shown in Figure 4e; and Figure S10, Supporting Information, the control group (no treatment), the "UV only" group (UV irradiation without NPs), and the "NPs only" group (NPs only without UV irradiation) show negligible cancer cell death. However, the therapy group treated by the NPs with the UV irradiation exhibits a cancer cell viability less than 10%, which confirms the therapeutic efficacy.

For the minimally invasive cancer treatment, the LMNs and flexible bioelectronics are integrated on the edge of the surgical forceps. The LMNs and the flexible device can be mounted on the tip or the side of the forceps depending on applications and surgical procedures (Figure 4f; and Figure S11a, Supporting Information, respectively). The flexible bioelectronics device

consists of the LMNs, an LED, a temperature sensor, electrical interconnects, and wire pads. The LMNs are placed on the LED (Figure 4f, inset) to assist the deep penetration of high-energy photons into target tumor tissues. The ultrathin temperature sensor is integrated under the LED to control the heat generated by the LED. Detailed layouts and magnified images of the bioelectronics are shown in Figure S11b,c, Supporting Information. The fabrication details are described in Methods Section and Figure S12, Supporting Information.

Figure 4g shows the wavelength-dependent intensity of the emitted light from the LED through LMNs (blue curve) and the typical light absorbance by the NPs (red curve). The wavelength for the peak of the emitted light and that for the light absorption by the NPs overlap each other. Therefore, the photons guided by LMNs can activate the NPs to generate ROS and release Dox. The electrical current applied to the LED is linearly correlated with the energy of light emitted from the LED (Figure 4h), and thus the light intensity can be precisely controlled.

Since the optical conversion efficiency of the LED is not 100%, the applied electrical energy to the LED is converted into both light and heat. The LED used in this study (SST-10-UV, LUMINUS, USA) has a peak wavelength of 365 nm and thermal resistance of 1.4 °C W^{-1}. The generated heat can raise the temperature of the artificial tissue by controlling the supplied power to the LED (Figure 4i). The target temperature of around 47 °C can be achieved with a current level of 200–240 mA (Figure S13a, Supporting Information). After the temperature sensor is calibrated (Figure S13b, Supporting Information), it can monitor the temperature of the artificial tissue during the heating (Figure S13c, Supporting Information). The time to reach the thermal steady state is less than 1 min (Figure S13d, Supporting Information). The heating by the LED can be monitored by the temperature sensor, and thus the facile control of the heating can be achieved (Figure 4j).

We evaluated the proposed method by using two types of animal models in vivo. After the subcutaneous implantation of glioblastoma (U-87 MG) and pituitary adenoma (AtT-20) cells to the immunocompromised mice, tumors were grown until their size of the long side becomes 5–7 mm. The experimental procedures are as follows (**Figure 5**). First, the skin covering the tumor is dissected to apply microneedles onto the tumor. BMNs are then applied to the tumor. BMNs are dissolved by biofluids, and theranostic NPs are released into the tumor. Then, LMNs on the bioelectronics deliver high-energy photons and activate the theranostic NPs (**Figure 6**a). MR imaging can be used to locate the NPs (Figure S14, Supporting Information). The heat generated by the LED accelerates the diffusion of the released therapeutic agents while the temperature is monitored by the temperature sensor. The treated tumor tissue is covered by the bioglue. Finally, the skin is covered, sutured, and disinfected. For the negative control group, the implanted tumor was exposed for the same period of time as the treatment group, and then sutured, and disinfected without applying BMNs and/ or LMNs.

The treatment efficacy of the glioblastoma model is assessed by monitoring the time-dependent change in the tumor volume via the T_2-weighted MR imaging (Figure 6b-d). The tumor volume of the negative control group has continuously increased over two weeks, while the tumor growth
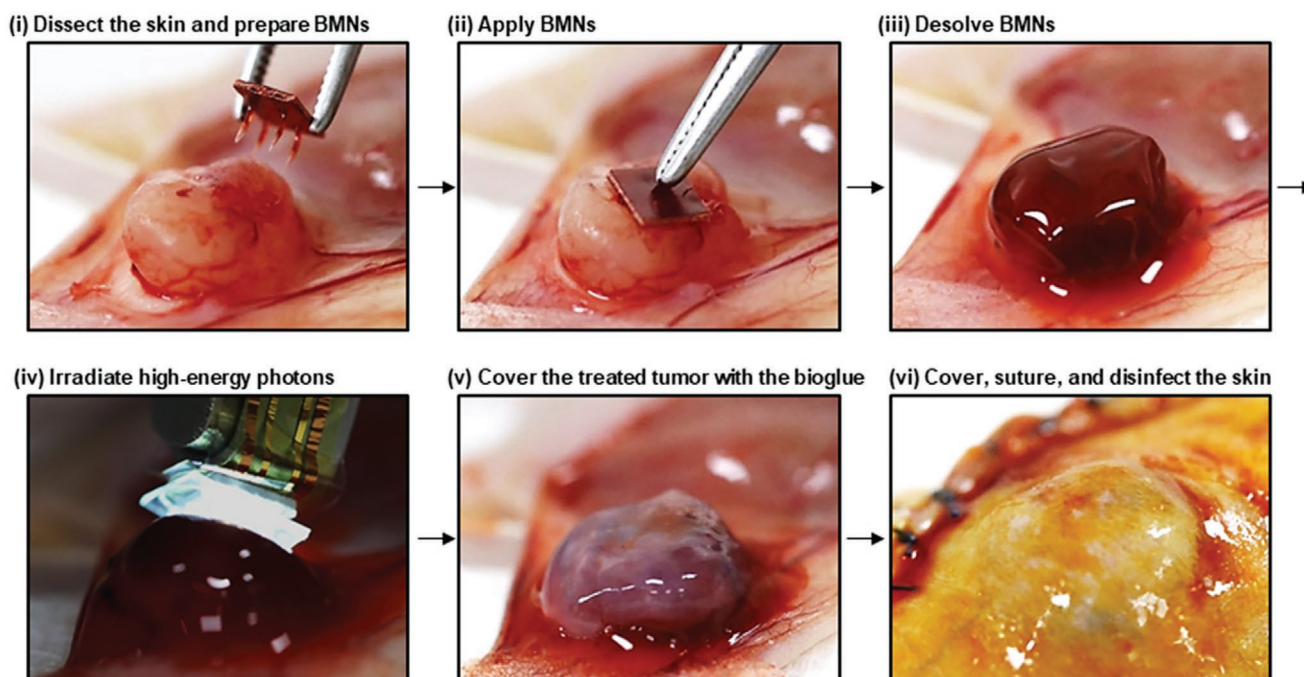
Figure 5. Surgical procedures for the demonstration of the proposed method. When the skin is incised and the tumor is exposed, the tumor is typically located on the interior skin. After BMNs are dissolved, the high-energy photons generated by the LED are delivered through the LMNs. Heat from the LED accelerates the diffusion of therapeutic moieties. Then, the treated surface of the tumor is covered by the bioglue. Finally, the skin and the tumor are restored (the treated side of the tumor faces inward), sutured, and disinfected.

has been suppressed in the therapy group during the monitoring period of two weeks after therapy (Figure 6e). After two weeks, the mean tumor volume change of the negative control group was 520%, whereas that of the therapy group was −12% (Figure 6f; $p = 0.0006$). This difference in the tumor volume results in a difference in the survival rate between two groups (Figure 6g; $p = 0.0001$). The therapy group had a median survival time of 42 days, 24 days longer than the negative control group. The treatment efficacy is confirmed by the haematoxylin and eosin (H&E) and terminal deoxynucleotidyl transferase dUTP nick-end labelling (TUNEL) staining (Figure 6h). More necrosis is observed in the therapy group than the control group. Also, the apoptosis of the deep tumor tissues is induced in the therapy group, while the control group shows no evidence of the apoptosis. Furthermore, the therapeutic efficacy of UV and heat only (without BMNs) was evaluated in the glioblastoma model (Figure S15, Supporting Information), demonstrating that the in vivo therapeutic effect of UV and heat only is limited.

As another demonstration, the same method was applied to the subcutaneous pituitary adenoma model. The treatment procedures for the pituitary adenoma model are the same as that of the glioblastoma model. After three weeks from the treatment, the suppression of the tumor growth is confirmed by the T_2-weighted MR imaging in the therapy group, while the notable tumor growth is observed in the negative control group (Figure 6i). Figure 6j shows the time-dependent change of the tumor volume over three weeks after the therapy. The negative control group has shown continuous tumor growth, while the therapy group has shown the suppression of the tumor growth. After three weeks, the mean tumor volume changes

show a large difference between the two groups (Figure 6k; $p = 0.0038$). These results are supported by the higher survival rate of the therapy group than that of the control group (Figure 6l; $p = 0.0004$).

The treatment efficacy of pituitary adenoma is confirmed further by analysing the hormone level, body weight, and skin condition. Pituitary adenoma produces an excessive amount of adrenocorticotropic hormone (ACTH) which causes Cushing's disease.[19] Therefore, the tumor growth and the consequent overproduction of ACTH accompany symptoms such as growth retardation, skin thinning, and skin keratinization.[19,20] The ACTH level in the plasma of the therapy group is much lower than that of the control group due to the suppression of the tumor growth (Figure 6m; $p = 0.0006$). Besides, the ACTH level of the therapy group exhibits a similar concentration compared to that of normal mice in the control group. The treatment recovers the body weight loss due to the high ACTH level (Figure 6n; $p = 0.0177$), and the thin and keratinized skin is rebounded to the normal skin condition after 4 weeks from the treatment (Figure 6o). The treatment efficacy of the pituitary adenoma model is confirmed by the H&E and TUNEL staining (Figure 6p). More necrosis and apoptosis of the tumor tissue are observed in the therapy group than the control group. The detailed procedure for the histology is the same as that for the glioblastoma model.

3. Conclusion

We propose a novel method for the localized delivery of theranostic NPs and high-energy photons using the
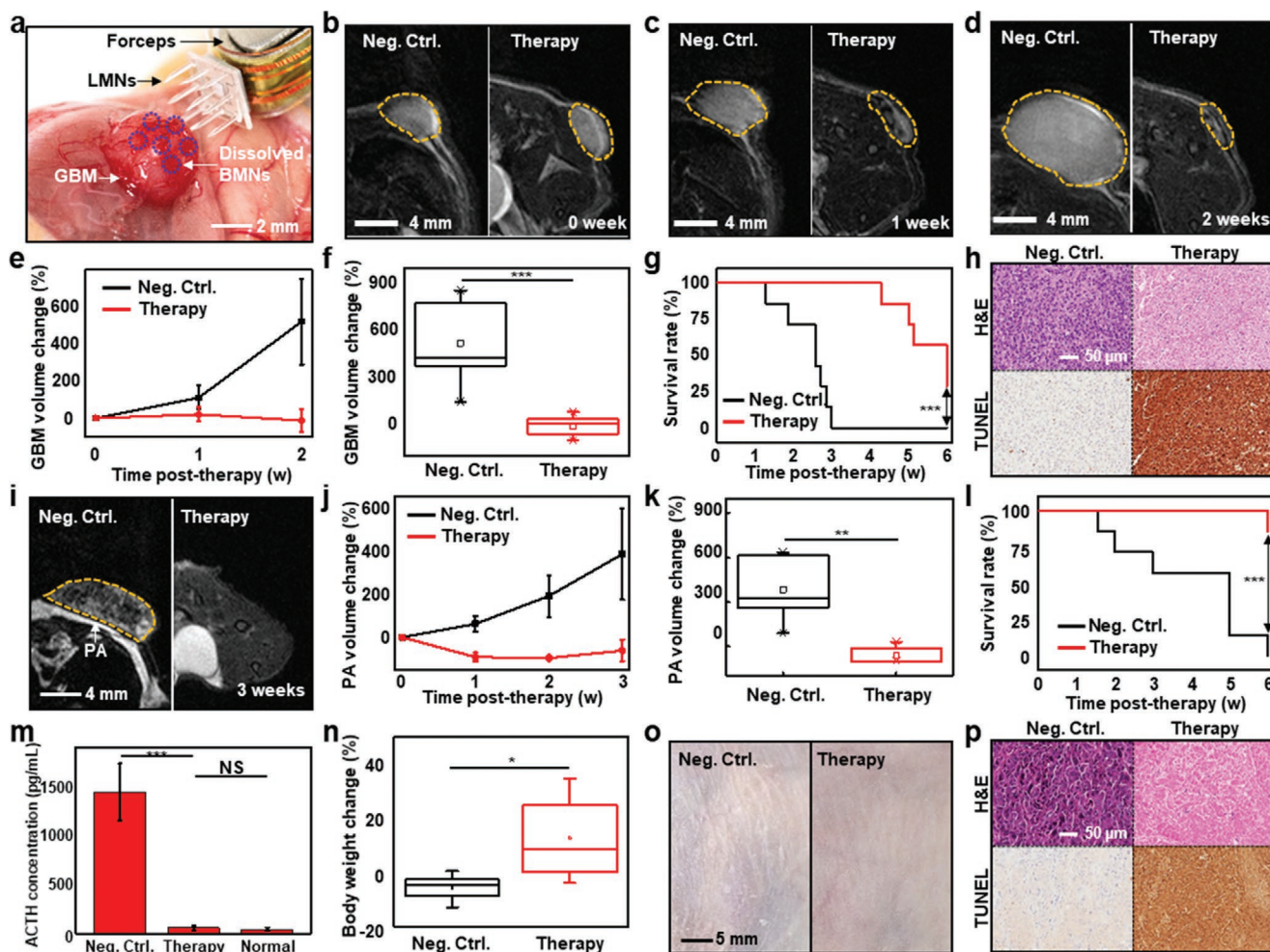
Figure 6. Demonstration of the proposed method by using subcutaneous brain tumor models in vivo. a) Image of the LMNs on the bioelectronics applied to the subcutaneous tumor model after the prior application of BMNs. b–d) MR images of the control group (left) and the therapy group (right) at 0 weeks (b), at 1 week after therapy (c), and at 2 weeks after therapy (d). e) Time-dependent glioblastoma volume change of the control and therapy group ($n_{Neg.Ctrl.} = 7$, $n_{Therapy} = 7$). f) Box-and-whisker plot of the glioblastoma volume of the control and therapy group at 2 weeks after therapy, Line: median, Box: 25th–75th percentiles, Whisker: min to max, ***$p < 0.001$ by Mann–Whitney U-test. g) Kaplan–Meier survival rate plot of two groups ($n_{Neg.Ctrl.} = 7$, $n_{Therapy} = 7$), ***$p < 0.001$ by log-rank test. h) Histology images of the glioblastoma tissue stained with H&E and TUNEL. i) MR image of the control group (left) and the therapy group (right) at 3 weeks after therapy, which shows the volume of pituitary adenoma. j) Time-dependent tumor (pituitary adenoma) volume change of the control and therapy group ($n_{Neg.Ctrl.} = 7$, $n_{Therapy} = 7$). k) Box-and-whisker plot of the tumor volume (right) of the control and therapy group at 3 weeks after therapy, Line: median, Box: 25th–75th percentiles, Whisker: min to max, **$p < 0.01$ by Mann–Whitney U-test. l) Kaplan–Meier survival rate plot of the control and therapy group ($n_{Neg.Ctrl.} = 7$, $n_{Therapy} = 7$), ***$p < 0.001$ by log-rank test. m) The ACTH concentration in the plasma of the pituitary adenoma model ($n_{Neg.Ctrl.} = 7$, $n_{Therapy} = 7$, $n_{Normal} = 3$) at 3 weeks after therapy, NS; $p > 0.05$, ***$p < 0.001$ by Mann–Whitney U-test, respectively. n) Body-weight change of two groups ($n_{Neg.Ctrl.} = 5$, $n_{Therapy} = 7$) at 3 weeks after therapy, *$p < 0.05$ by Mann–Whitney U-test. o) Image of the skin for the negative control (left) and therapy (right) group. p) Histology images of the pituitary adenoma tissue stained with H&E and TUNEL.

microneedles-on-bioelectronics. The theranostic NPs were released from BMNs locally and activated by high-energy photons guided by LMNs on the bioelectronics. The activated theranostic NPs generate cytotoxic ROS and released Dox, and the thermal actuation controlled by the bioelectronics accelerates the diffusion of the released therapeutic moieties. We have demonstrated our delivery and activation method with brain tumor models in vivo. The tumor growth was suppressed and the survival rate was increased. Further studies including the optimization of the microneedle designs, the development of advanced multifunctional bioelectronics,[21] and the optimization of the application protocols are required in the future. The inte-

gration of these systems with medical devices such as an endoscope can facilitate access to tumors located at internal organs.

4. Experimental Section

A detailed description of procedures and characterization methods can be found in the Supporting Information.

Supporting Information

Supporting Information is available from the Wiley Online Library or from the author.

Conflict of Interest

The authors declare no conflict of interest.

Data Availability Statement

Research data are not shared.

[1] a) D. Shae, K. W. Becker, P. Christov, D. S. Yun, A. K. R. Lytton-Jean, S. Sevimli, M. Ascano, M. Kelley, D. B. Johnson, J. M. Balko, J. T. Wilson, *Nat. Nanotechnol.* **2019**, *14*, 269; b) Q. Zhou, S. Q. Shao, J. Q. Wang, C. H. Xu, J. J. Xiang, Y. Piao, Z. X. Zhou, Q. S. Yu, J. B. Tang, X. R. Liu, Z. H. Gan, R. Mo, Z. Gu, Y. Q. Shen, *Nat. Nanotechnol.* **2019**, *14*, 799.

[2] a) C. Liang, S. Diao, C. Wang, H. Gong, T. Liu, G. Hong, X. Shi, H. Dai, Z. Liu, *Adv. Mater.* **2014**, *26*, 5646; b) Y. Dai, H. Xiao, J. Liu, Q. Yuan, P. a. Ma, D. Yang, C. Li, Z. Cheng, Z. Hou, P. Yang, J. Lin, *J. Am. Chem. Soc.* **2013**, *135*, 18920; c) N. M. Idris, M. K. Gnanasammandhan, J. Zhang, P. C. Ho, R. Mahendran, Y. Zhang, *Nat. Med.* **2012**, *18*, 1580.

[3] a) C. D. Arvanitis, G. B. Ferraro, R. K. Jain, *Nat. Rev. Cancer* **2020**, *20*, 26; b) W. A. Banks, *Nat. Rev. Drug Discovery* **2016**, *15*, 275.

[4] Z. R. Stephen, F. M. Kievit, O. Veiseh, P. A. Chiarelli, C. Fang, K. Wang, S. J. Hatzinger, R. G. Ellenbogen, J. R. Silber, M. Q. Zhang, *ACS Nano* **2014**, *8*, 10383.

[5] a) L. Li, Z. Yang, S. J. Zhu, L. C. He, W. P. Fan, W. Tang, J. H. Zou, Z. Y. Shen, M. R. Zhang, L. G. Tang, Y. L. Dai, G. Niu, S. Hu, X. Y. Chen, *Adv. Mater.* **2019**, *31*, 1901187; b) R. Weissleder, *Nat. Biotechnol.* **2001**, *19*, 316; c) H. Wang, Z. Gao, X. Liu, P. Agarwal, S. Zhao, D. W. Conroy, G. Ji, J. Yu, C. P. Jaroniec, Z. Liu, X. Lu, X. Li, X. He, *Nat. Commun.* **2018**, *9*, 562.

[6] a) J. A. Liu, W. B. Bu, L. M. Pan, J. L. Shi, *Angew. Chem., Int. Ed.* **2013**, *52*, 4375; b) H. Q. Chu, J. Zhao, Y. S. Mi, Z. H. Di, L. L. Li, *Nat. Commun.* **2019**, *10*, 2839.

[7] M. Kim, J. An, K. S. Kim, M. Choi, M. Humar, S. J. J. Kwok, T. H. Dai, S. H. Yun, *Biomed. Opt. Express* **2016**, *7*, 4220.

[8] a) I. V. Martynenko, A. O. Orlova, V. G. Maslov, A. V. Baranov, A. V. Fedorov, M. Artemyev, *Beilstein J. Nanotechnol.* **2013**, *4*, 895; b) T. Hatakeyama, Y. Murayama, S. Komatsu, A. Shiozaki, Y. Kuriu, H. Ikoma, M. Nakanishi, D. Ichikawa, H. Fujiwara, K. Okamoto, T. Ochiai, Y. Kokuba, K. Inoue, M. Nakajima, E. Otsuji, *Oncol. Rep.* **2013**, *29*, 911.

[9] a) E. Caffarel-Salvador, S. Kim, V. Soares, R. Y. Tian, S. R. Stern, D. Minahan, R. Yona, X. Y. Lu, F. R. Zakaria, J. Collins, J. Wainer, J. Wong, R. McManus, S. Tamang, S. McDonnell, K. Ishida, A. Hayward, X. W. Liu, F. Hubalek, J. Fels, A. Vegge, M. R. Frederiksen, U. Rahbek, T. Yoshitake, J. Fujimoto, N. Roxhed, R. Langer, G. Traverso, *Sci. Adv.* **2021**, *7*, eabe2620; b) W. Chen, B. Cai, Z. Geng, F. Chen, Z. Wang, L. Wang, X. Chen, *Matter* **2020**, *3*, 1589.

[10] C. C. Winterbourn, *Nat. Chem. Biol.* **2008**, *4*, 278.

[11] J. Lee, H. R. Cho, G. D. Cha, H. Seo, S. Lee, C. K. Park, J. W. Kim, S. T. Qiao, L. Wang, D. Kang, T. Kang, T. Ichikawa, J. Kim, H. Lee, W. Lee, S. Kim, S. T. Lee, N. S. Lu, T. Hyeon, S. H. Choi, D. H. Kim, *Nat. Commun.* **2019**, *10*, 5205.

[12] a) S. L. Asa, S. Ezzat, *Nat. Rev. Cancer* **2002**, *2*, 836; b) A. Beckers, P. Petrossians, J. Hanson, A. F. Daly, *Nat. Rev. Endocrinol.* **2018**, *14*, 705.

[13] a) A. Di Ieva, F. Rotondo, L. V. Syro, M. D. Cusimano, K. Kovacs, *Nat. Rev. Endocrinol.* **2014**, *10*, 423; b) J. A. Gondim, J. P. C. Almeida, L. A. F. Albuquerque, M. Schops, E. Gomes, T. Ferraz, W. Sobreira, M. T. Kretzmann, *Pituitary* **2011**, *14*, 174.

[14] D. Chauvet, M. Imbault, L. Capelle, C. Demene, M. Mossad, C. Karachi, A. L. Boch, J. L. Gennisson, M. Tanter, *Ultraschall Med.* **2016**, *37*, 584.

[15] Z. J. Chen, G. T. Gillies, W. C. Broaddus, S. S. Prabhu, H. Fillmore, R. M. Mitchell, F. D. Corwin, P. P. Fatouros, *J. Neurosurg.* **2004**, *101*, 314.

[16] M. R. Querry, *Optical Constants, Contractor report*, US Army Chemical Research, Development and Engineering Center (CRDEC), Aberdeen Proving Ground, MD, USA **1985**.

[17] W. Hergert, T. Wriedt, *The Mie Theory: Basics and Applications*, Springer, Berlin, Germany **2012**.

[18] a) C. de Gracia Lux, C. L. McFearin, S. Joshi-Barr, J. Sankaranarayanan, N. Fomina, A. Almutairi, *ACS Macro Lett.* **2012**, *1*, 922; b) L. Sun, X. F. Ma, C. M. Dong, B. S. Zhu, X. Y. Zhu, *Biomacromolecules* **2012**, *13*, 3581.

[19] H. Fukuoka, O. Cooper, A. Ben-Shlomo, A. Mamelak, S. G. Ren, D. Bruyette, S. Melmed, *J. Clin. Invest.* **2011**, *121*, 4712.

[20] S. Murasawa, K. Kageyama, A. Sugiyama, N. Ishigame, K. Niioka, T. Suda, M. Daimon, *Mol. Cell. Endocrinol.* **2014**, *394*, 37.

[21] a) H. A. Ledesma, X. J. Li, J. L. Carvalho-de-Souza, W. Wei, F. Bezanilla, B. Z. Tian, *Nat. Nanotechnol.* **2019**, *14*, 645; b) Y. Zhang, D. C. Castro, Y. Han, Y. X. Wu, H. X. Guo, Z. Y. Weng, Y. G. Xue, J. Ausra, X. J. Wang, R. Li, G. F. Wu, A. Vazquez-Guardado, Y. W. Xie, Z. Q. Xie, D. Ostojich, D. S. Peng, R. J. Sun, B. B. Wang, Y. Yu, J. P. Leshock, S. B. Qu, C. J. Su, W. Shen, T. Hang, A. Banks, Y. G. Huang, J. Radulovic, P. Gutruf, M. R. Bruchas, J. A. Rogers, *Proc. Natl. Acad. Sci. USA* **2019**, *116*, 21427; c) A. Bansal, F. Y. Yang, T. Xi, Y. Zhang, J. S. Ho, *Proc. Natl. Acad. Sci. USA* **2018**, *115*, 1469; d) S. Park, Y. Y. Guo, X. T. Jia, H. K. Choe, B. Grena, J. Kang, J. Park, C. Lu, A. Canales, R. Chen, Y. S. Yim, G. B. Choi, Y. Fink, P. Anikeeva, *Nat. Neurosci.* **2017**, *20*, 612.